Induction thermography of steel coupons with cracks

Genest, Marc; Li, Gang

Publisher's version / Version de l'éditeur:
https://doi.org/10.1364/AO.57.000D40
Applied Optics, 57, 18, pp. D40-D48, 2018-03-16

applied optics

Induction thermography of steel coupons with cracks

Marc Genest* and Gang Li

Aerospace Research Centre, National Research Council Canada, 1200 Montreal Rd, Bldg. M14, Ottawa, Ontario K1A 0R6, Canada
*Corresponding author: marc.genest@nrc-cnrc.gc.ca

Received 22 December 2017; revised 18 February 2018; accepted 18 February 2018; posted 20 February 2018 (Doc. ID 318304); published 16 March 2018

The induction thermography technique was assessed experimentally and numerically on notched steel coupons using two coil configurations: straight line and loop conditions. The coupons had different lengths of fatigue crack varying from zero to 3 mm. The numerical predictions showed that the peak temperature was always located at the crack tip or the notch tip position. The loop coil resulted in higher temperatures than those of the straight line coil. Results showed that the numerical methods effectively supported the application assessment of this nondestructive evaluation (NDE) technique for the steel material, but crack geometry remains a challenge as the exact shape of a natural crack is typically unknown. It is shown that induction thermography can detect a crack as small as 1 mm in the notched steel coupons. Commentary on the application of the NDE technique with the numerical modeling support was provided.

OCIS codes: (120.4290) Nondestructive testing; (110.6820) Thermal imaging; (110.3080) Infrared imaging.

https://doi.org/10.1364/AO.57.000D40

1. INTRODUCTION

Induction heating is the process of heating an electrically conductive object by electromagnetic induction, where induced currents are generated within the test piece and electrical resistance leads to heating of the test piece. Induction thermography is a nondestructive evaluation (NDE) technique that uses induction heating for detection of flaws in conductive materials and has been used since the 1980s [1]. This technique has potentials to improve the inspection speed and ease the visualization of flaw detection in complex geometries with the aid of infrared (IR) cameras. IR cameras can accurately detect real-time temperature profile on the test piece surface and small temperature gradient caused by the presence of flaws. Over the last decade, this nondestructive test method has gained more and more interest and has been used on both metallic and carbon or boron fiber reinforced composite materials [2–6].

During the induction heating process, nonlinear temperature-dependent material properties may be exhibited in the heated materials due to potentially large temperature change [7,8]; although, this nonlinearity seldom is a real issue in NDE applications, as those are typically performed at relatively low temperature (below 60°C). For complex geometry, it is difficult to obtain analytical solutions for identifying the electromagnetic and temperature distributions. Therefore, numerical methods such as the multiphysics finite element (FE) methods are applied for the investigation. Currently, most existing papers in the open literature [9–14] are using finite element methods that are limited to a two-dimensional (2D) condition for specific case evaluations. The 2D axisymmetric models can rapidly assess the setup efficiency under the influence of preferred elements, such as coil dimension, distance between the test piece and the coil, current intensity, etc. Due to the model limitation, the 2D models cannot study the temperature in a test piece of complex shape and the geometry of crack or flaw contained inside the test piece cannot be studied in a 2D condition [15–20]. To this end, three-dimensional (3D) modeling capability was developed to support NDE thermography applications of metallic panels [21]. In this study, the 3D finite element models were created using COMSOL Multiphysics software version 5.1 for simulating the induction heating of notched steel coupons with different crack lengths. Through comparing the temperature profiles and temperature maps obtained, application of the induction thermography technique on the steel coupons is discussed.

2. THEORY AND EXPERIMENTAL DETAILS

A. Theoretical Background

Mathematical equations describing the electromagnetic phenomena involved in induction heating are given by the Maxwell's equations. According to Ampere's law (last of Maxwell's equations), an alternating coil current flowing through a wire or coil will produce an alternating magnetic field of the same frequency as the source current. The electromagnetic field's strength will depend on the coil current, coil

geometry, and distance from the coil. The alternating magnetic field induces current in the test conductive piece located near the coil. The induced current is in opposite direction of the coil current. The associated field equations can be found elsewhere [22].

B. Experimental Details

A commercial induction heating system, the Easyheat 2.4 from Ambrell, was employed in the experimental investigation. The system has an induction heating control box that supplies up to 2.4 kW of power to the work head. A copper coil excited by the work head is placed in proximity of the test piece surface to create induction heating of the test piece. Water is circulated through the coil using a water to air heat exchanger during the experiments to maintain the coil element cool at a flow rate of $Mt = 1.2$ kg/min. Thus, the heat transfer is mainly inductive and there is minimal radiation transfer from the coil to the test piece. The temperature distributions on the test piece coil side were captured by an IR camera (FLIR SC3000), which has a 320 × 240 pixel array, a maximum full frame rate of 60 Hz, and noise equivalent temperature difference of ~20 mK.

The test pieces investigated during this study were notched 2.7 mm thick AISI type O1 steel coupons made according to ASTM E399-05 standard. Each specimen has a length and width of 143 and 137 mm, respectively. The samples were fatigued to generate controlled nominal crack lengths of 0.1, 1, 2, and 3 mm using a tension-tension sinusoidal fatigue load of 15.5 kN at the frequency of 10 Hz and at the stress ratio (R) of 0.1 [23]. The final cracks lengths measured optically were 0.2, 0.78, 1.75, and 3.14 mm with a crack width of approximately 0.005 mm. One sample was kept as manufactured without crack as a reference coupon. The samples were painted black with high emissivity coefficient paint (~0.95) that was used neglect the reflection issue typical with low emissivity of bare metal. Paint thickness varied slightly from sample to sample from 16 to 26 μm and the effect of this thickness variation on the temperature measurements was deemed negligible.

Experiments were carried out using two different coil configurations: a straight coil and three-loop coil. The steel coupon geometry with the coil setups is shown in Figs. 1 and 2. In the straight coil configuration, a hollow copper tube was placed approximately 10 mm away in the front of the samples. The copper coil, 6.35 mm outer diameter and 1.2 mm wall thickness, was placed perpendicular to the notch and the crack, with its side aligned with the notch tip. Induction heating was carried out for a duration of 0.5 s using three different current intensities: 100, 150, and 200 A at a frequency that was around 300 kHz (294–301 kHz). In the three-loop coil configuration, the loops were centered over the notch tip. Since this coil configuration generates significantly more electromagnetic fields, the current intensities were reduced to 25, 50, and 100 A, while the excitation duration remained at 0.5 s, and the frequency was around 300 kHz, varying from 291 kHz to 320 kHz, with higher frequency being used for lower current, and lower frequency at higher current due to the self-tuning nature of the induction system.

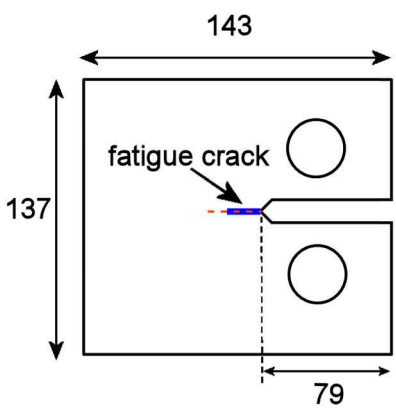

Fig. 1. Schematic drawing of the notched coupon (dimension in millimeters).

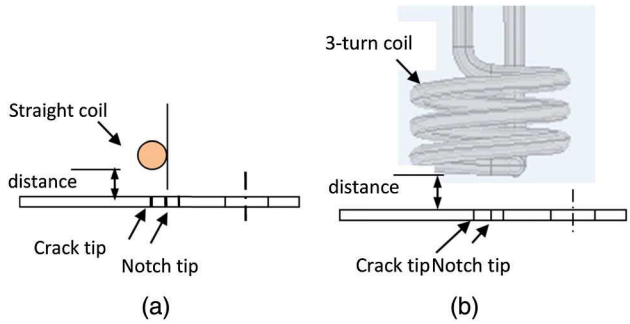

Fig. 2. Side view showing the (a) straight coil and (b) three-loop coil setups and positions.

3. MULTIPHYSICS FINITE ELEMENT MODELING

A. Multiphysics Model Setup

COMSOL Multiphysics software version 5.1 was used to create the 3D induction heating FE models that included four domains: air, steel sample, coil, and water. Two coupling multiphysics—magnetic field (MF) and heat transfer in solids—were used in the induction heating simulation. The electric power in the MF was setup through boundary conditions using "lumped port" and "impedance boundary condition" provided by the software. The electrical current intensity was supplied to one end section of the coil exterior boundaries via the "lumped port," while the remaining of the coil exterior boundaries were set to "impedance boundary conditions." The initial ambient temperature was 23°C.

A model for the steel sample with a straight line coil is shown in Fig. 3. The path highlighted by the red line in Fig. 3(b) (red dashed line in Fig. 1) on the sample coil side (outer) surface was used to study the temperature profiles. In this model, the air domain dimension, 200 mm × 170 mm × 150 mm, covers the entire system. The other model with a three-loop coil system is shown in Fig. 4. In the three-loop coil system model, the loop outer diameter was 50 mm with 3.18 mm spacing between the loops, and the air domain dimension was 140 × 150 × 180 mm. To reduce the computation time, only a section of the steel sample was modeled covering the area of interest around the notch and the crack. The dimension of the steel coupon modeled was 80 mm × 60 mm × 2.7 mm. The reduced selected section does not affect the induced temperatures in the notched coupon region. Two types of elements

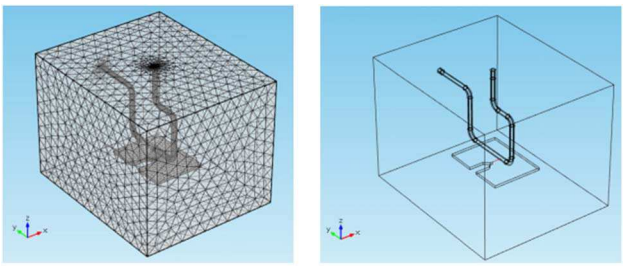

(a) (b)

Fig. 3. Three-dimensional (3D) FE model for the notched steel coupon induced by a straight coil for (a) meshed condition and (b) a surface path along the crack direction for temperature assessment.

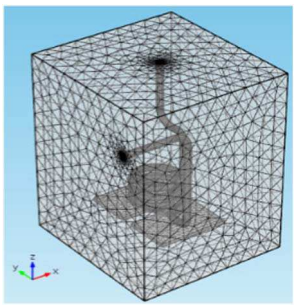

Fig. 4. Three-dimensional (3D) FE model for the notched steel coupon induced by a three-loop coil system.

were used to mesh the model. Tetrahedral elements between the 1 mm and 15 mm size were customized for meshing coupon, water, and air domains. For the steel crack position, very fine size from 0.6 mm to 11 mm was used to ensure the mesh condition. Triangular elements in the predefined "fine" size with the minimum of 2 mm and maximum of 16 mm in size were used to mesh the coil exterior boundaries. The number of generated elements was slightly over 112,000 for the straight line coil models and 226,000 for the three-loop coil model. All the simulations were conducted in a laptop equipped with the Intel core i7-4800 MQ CPU at 2.7 GHz and 32 GB RAM. A case simulation took approximately 8 min for the straight coil model and 18 min for the three-loop coil model for a 0.5 s heating period with a 0.05 s time increment.

B. Material Parameters

Table 1 gives the material properties used in the numerical analyses. Since the exact material parameters of the steel for relative permeability and thermal conductivity were not known, two values for each of the two parameters were selected based on value scatter found in the literature. The water thermal conductivity (k) was set to 1000 W/(m K) in the numerical model to account for the turbulent flow of water.

4. RESULTS

A. Straight Coil

Experiments with the line coil were carried out using 100, 150, and 200 A current intensities, with coil located 10 mm away from the surface. A comparison of the full-field temperature obtained from experiment and modeling are presented in Fig. 5 for a 2 mm crack using 100 A current at the 0.5 s heating time. It can be seen that a similar temperature distribution was obtained from the two methods. With a shorter distance to the coil system, a higher temperature gradient at the crack locations was created than that of other locations.

Experimentally, the temperatures observed by the IR camera were much higher on the sample with a 2 mm crack than other samples. An explanation for that higher temperature is provided further at the end of this section, and was identified after the data had been processed. To compensate for this observation, the full-field temperature images and relevant path temperature profiles are presented using a normalized temperature and contrast from normalized temperature. Experiments were carried out using three different induction heating times: 100, 250, and 500 ms. Experimental and numerical results showed a high temperature increase at the notch tip, regardless of the presence of a crack. This was due to the geometry of the samples, which results in a concentration of electromagnetic field at the notch

Table 1. Material Parameters Used in the Numerical Models

Material Parameter	Air	Copper	Water	Steel[a]
Relative permeability, μ_r	1	1	1	100/1000
Relative permittivity, ε_r	1	1	80	1
Electrical conductivity, σ (S/m)	α	5.998E7	5.5E−6	4.E+6
Specific heat, C_p (J/kg K)	default[b]	385	default	435
Density, ρ (kg/m^3)	default	8700	default	7850
Thermal conductivity, k (W/(m K)	default	400	1000[c]	15/45

[a]Referring to http://www.engineeringtoolbox.com/permeability-d_1923.html (cited in Feb. 2017) on the relative permeability of the martensitic stainless steel is from 750 to 950 for the annealed and 40–95 for the hardened; therefore, 100 and 1000 are selected in the model individually. Also referring to https://www.engineersedge.com/properties_of_metals.htm (cited in Feb. 2017), the thermal conductivity is quite wide from 16.26 (stainless 316) to 63.9 (SAE 1010 sheet); hence this parameter in 15 and 45 is selected individually.

[b]"Default" refers to the relevant temperature-dependent values provided by the software material library.

[c]The 1000 W/(m K) thermal conductivity is for the turbulent flow of water.

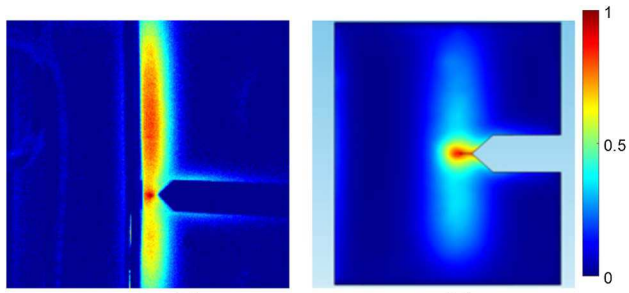

(a) (b)

Fig. 5. Full-field temperature increase induced by 100 A current at 0.5 s heating time obtained from (a) experimental and (b) numerical methods.

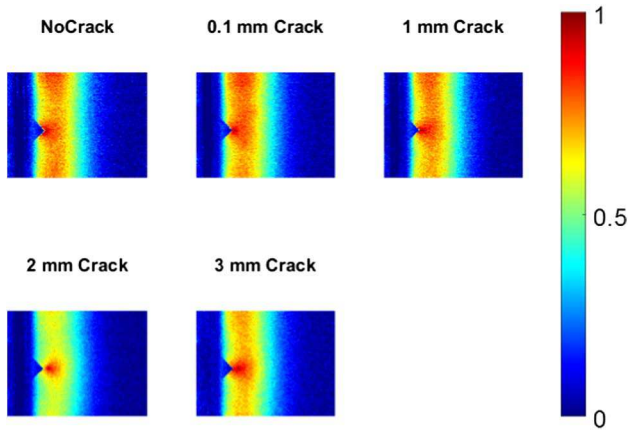

Fig. 6. Normalized temperature increase induced by the straight line coil with the 100 A at the 500 ms heating time.

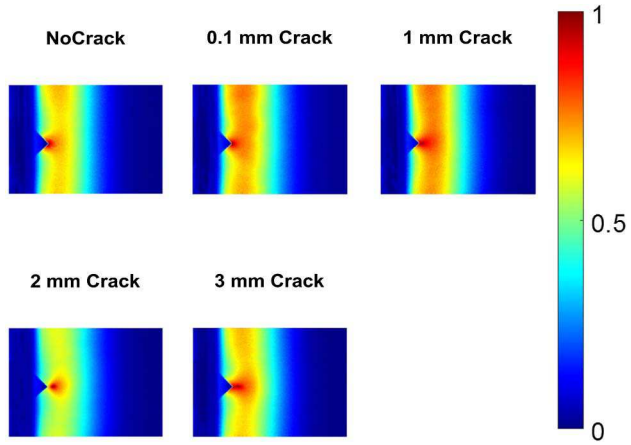

Fig. 8. Line coil normalized temperature increase with the 200 A at the 250 ms heating time.

tip [22]. In the normalized temperature results obtained for a 100 A at the 500 ms excitation time (Fig. 6), only the 2 mm crack seemed visible, while the 0.1, 1, and 3 mm cracked samples behaved similarly to the reference sample (no crack).

Further signal processing consisted of subtracting temperature obtained for the reference coupon from that of the crack coupons, and the normalized temperature difference data was performed using a processing technique called differential thermography [24–26] for enhancing the crack detection capability. Although this additional processing did not yield significant improvement in terms of crack detection for the 100 A test, as shown in Fig. 7, the results from the 0.1 and 1 mm cracks confirmed that the temperature rise observed from the normalized temperatures was mainly due to the notched geometry rather than the presence of cracks.

Experimental results, full-field temperature maps, and temperature profiles were assessed for additional 150 and 200 A current intensities at the 100, 250, and 500 ms heating moments. Similar observations as that of the 100 A were obtained: stronger thermal contrast being obtained at higher current intensity; by increasing the current from 100 A to 200 A, the thermal contrast increased by fourfold. Only the 2 and 3 mm long cracks were detected using the differential thermography technique. Also, it was noticed that shorter heating time resulted in higher thermal gradient at the flawed locations, and thus highlighted the importance of minimizing and optimizing the heating time, as the material thermal conductivity rapidly diffuses the heat being generated by a flaw and thus blurs the crack indication in the temperature images as time goes by. To illustrate the importance of differential thermography, typical results obtained for a 200 A at the 250 ms heating time are presented in Figs. 8 and 9.

Several simulations were carried out to predict path temperature profiles. To highlight the influence of the material properties, the relative permeability (μ_r) of steel was set to 1000 while the thermal conductivity (k) was set at 15 and 45 W/(m K). The 200 A current intensity increased almost 3 times in the temperature magnitude as compared to that of the 100 A current intensity. The 45 W/(m K) thermal conductivity lowered the temperature by approximately half in the sample as compared to that of the 15 W/(m K) thermal conductivity used, since the higher conductivity dissipated heat faster to the surrounding areas. The observed common feature is that the peak

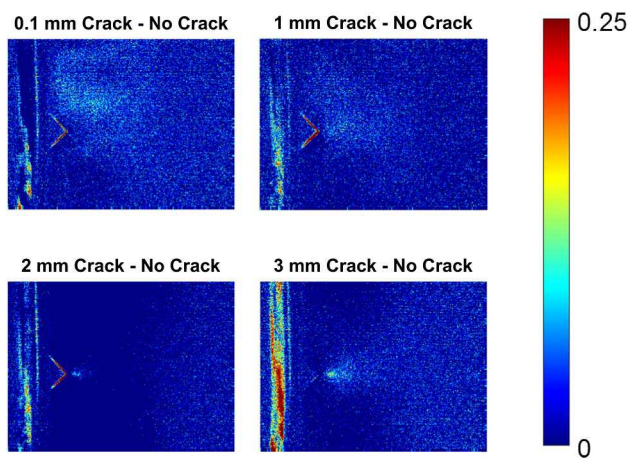

Fig. 7. Line coil temperature difference from reference with the 100 A at the 500 ms heating time.

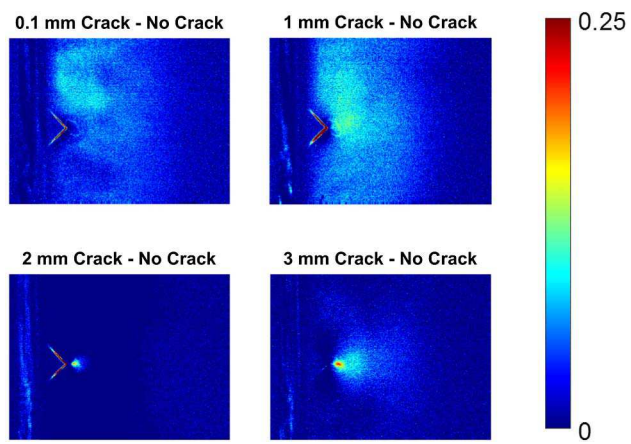

Fig. 9. Line coil temperature difference from reference sample with the 200 A at the 250 ms heating time.

temperature is always located at the notch tip for the no cracked sample or the crack tip for the cracked samples, regardless of the current intensity or material properties.

Comparisons between the experimental and numerical temperature profiles along the path for a 200 A current are shown in Fig. 10. Reasonable agreement in the temperature variations was obtained between the experimental and numerical results with a relatively better agreement obtained for the coupon with a 2 mm long crack.

Numerical results showed that (i) high relative permeability and current intensity generated high temperatures, and (ii) the peak temperature located at the crack tip, and high temperature was also located at the notch tip. With regard to the material parameters, relative permeability (100 and 1000) and thermal conductivity (15 and 45 W/(m K)), the numerical analyses aimed to cover the experimental results. The experimental results showed that (i) the peak temperature was not at the actual tip position (except the 2 mm long crack case), and (ii) the temperature rise for the coupon with a 3 mm long crack was lower than the coupons with the 1 mm and 2 mm long cracks, not as expected as that high temperature was created by the long crack. The discrepancies between the experimental and numerical results could results from two major aspects: (i) inaccurate material parameters used in the numerical analyses, although the actual material parameter was covered by the model; and (ii) differences between the actual crack (direction and crack gap size). Microscope images of the 1, 2, and 3 mm long cracks are shown in Fig. 11. From those images one can

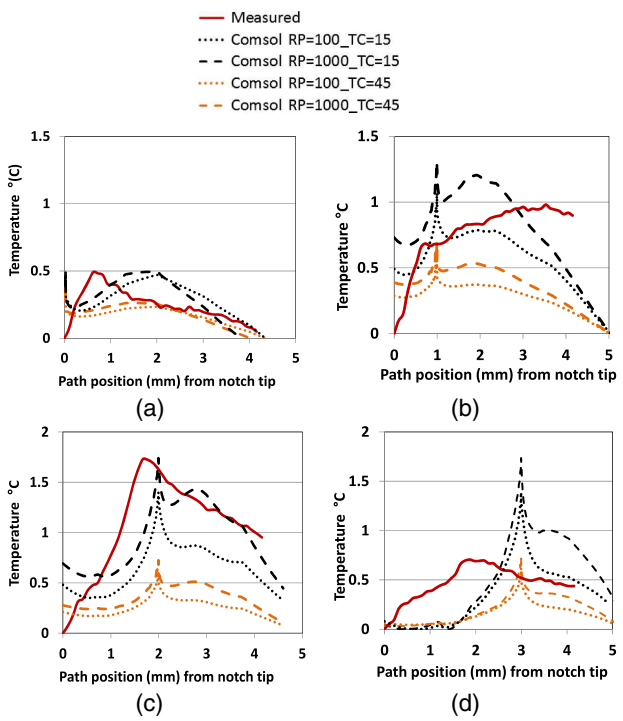

Fig. 10. Comparisons of the temperature rises along the surface path obtained from experimental measurements and numerical predictions at the 0.5th second heating time for: (a) no crack, (b) 1 mm long crack, (c) 2 mm long crack, and (d) 3 mm long crack for a 200 A current intensity.

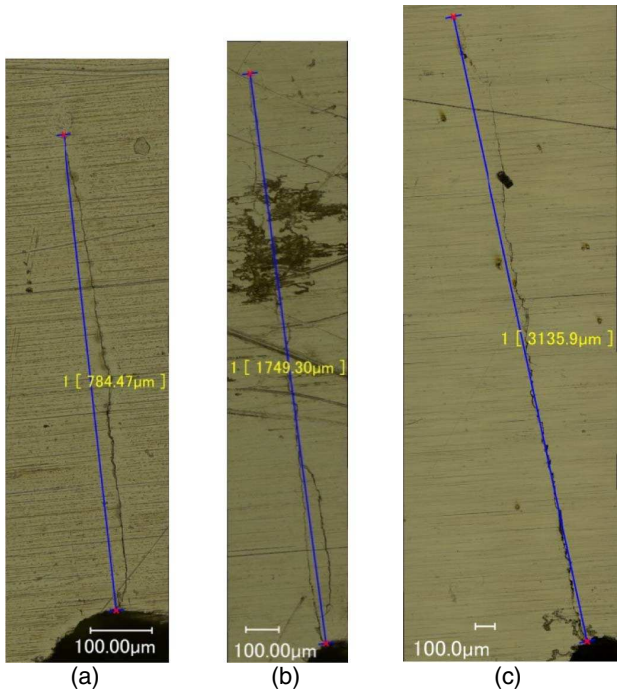

Fig. 11. Images for showing actual conditions of the crack starting at the coupon notch tip.

clearly see that the crack width varies over the crack length and become very narrow close to the position where the peak temperature was measured in the 3 mm crack. Another major observation was that the 2 mm crack bifurcates and merged back in to a single crack. This bifurcation may be the major reason why the amount of heat measured by the IR camera was much higher than the others. A third observation was that the actual cracks were not exactly at the 90° position path as assumed in the model; consequently, the path for measuring the temperatures and numerical modeling were slightly different. Also, it can be seen that the peak temperatures for the 2 and 3 mm cracks were clearly higher than the rest of the temperatures, while the peak temperature for the 1 mm crack was similar to its surrounding temperatures, presented in the model, and made it is harder to be detected. Results showed that the detection capabilities using a straight line configuration for steel seemed limited to the cracks that were at least 2 mm long.

B. Three-Loop Coil

The electromagnetic field generated from the three-loop coil system is proportional to the current and the number of turn on the coils; thus the field is inherently stronger than that of a straight coil for the same current due to its geometry. Thus, it yields higher temperature at the notch tip and crack region. Since there is no need to have excessive heat generated for NDE purpose, the experiments using the tree-loop coil were carried out using current intensities of 25, 50, and 100 A.

As in the straight coil configuration, the temperature measurements were normalized and differential thermography was performed to increase the flaw contrast at three heating times: 100, 250, and 500 ms. Measured temperature induced by a

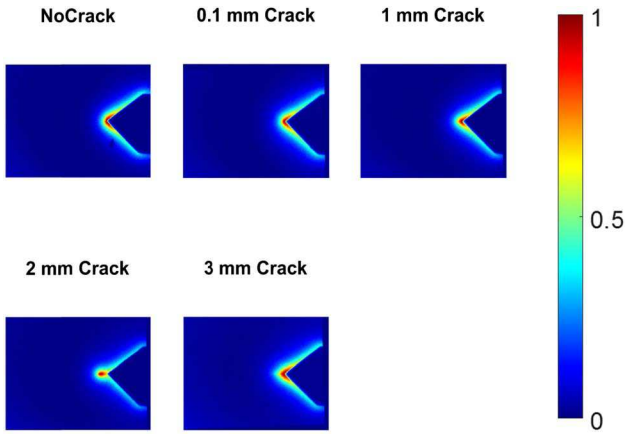

Fig. 12. Images for the three-loop coil normalized temperature increase with the 50 A current at the 100 ms heating time.

50 A current at the 100 ms heating time are shown in Figs. 12 and 13.

Similar observations as the straight coil were obtained in this section. The normalized temperature results (Fig. 12) showed that a high temperature increase was generated at the notch tip, regardless of the presence of a crack. Only the 2 mm crack was clearly discernible, while the 0.1, 1, and 3 mm cracked coupons behaved similarly to the reference sample (no crack). From the temperature measurements, it was also noticed that the presence of the 2 mm crack sample was sharper and better identified at the 100 ms than the 250 and 500 ms heating times.

The normalized temperature difference data, obtained using differential thermography [24] (normalized temperature of cracked sample subtracted by the normalized temperature of reference sample) enhances the crack detection capability. As can be seen in Fig. 13, the 1, 2, and 3 mm cracks became visible. It was noticed that the signal-to-noise ratio increased with high current intensities applied. Again, an earlier observation time yielded stronger contrast. Based on the results, we are confident that a 1 mm crack in steel can be detected using the induction thermography with the looped coil system.

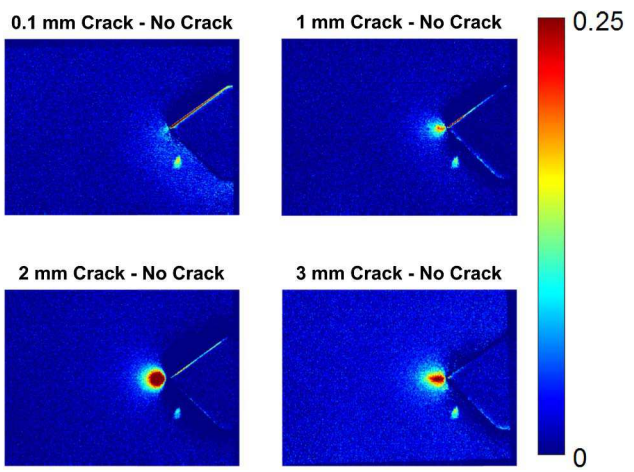

Fig. 13. Three-loop coil temperature difference from the reference sample with the 50 A current at time 100 ms heating time.

Results showed that a 100 A excitation considerably reduced the influence of the signal noise on the crack detection capability, and increase the thermal contrast of the flaw by over 15 times compared to the 25 A. Also, it is recommended to look at short heating time periods such as 100 and 250 ms for a better contrast.

1. Comparisons of the Experimental and Numerical Results

Temperature profiles for the three-loop coil were modeled along the same path as for the straight line coil for 50 A and 100 A current intensities. In those simulations, the relative permeability used for the steel samples was 1000 and the thermal conductivity was 15 and 45 W/(m K). Similar observations as those of the straight coil were obtained. The 100 A current intensity increased the temperature by more than 3 times that obtained with the 50 A current intensity. The 45 W/(m K) thermal conductivity lowered approximately by half the temperature increase compared to that of the small thermal conductivity of 15 W/(m K) condition. The peak temperature was always located at the notch tip for the no crack coupon or the crack tip for the cracked coupons. Also, a noticeable observation was that the maximum temperatures measured were similar regardless of the different crack lengths. In addition, for the same 100 A current intensity, the magnitude of the temperature increase created by the three-loop coil was more than 12 times than the one obtained using the straight line coil condition.

Comparisons between the experimental and numerical temperature profiles along the path are shown in Fig. 14. Again, fairly good agreement in the temperature variations and trends was obtained between the experimental and numerical results. Relatively better agreement was obtained for the coupon with a 2 mm long crack, and reasonable agreement was obtained for other crack conditions. Similar features were obtained using the

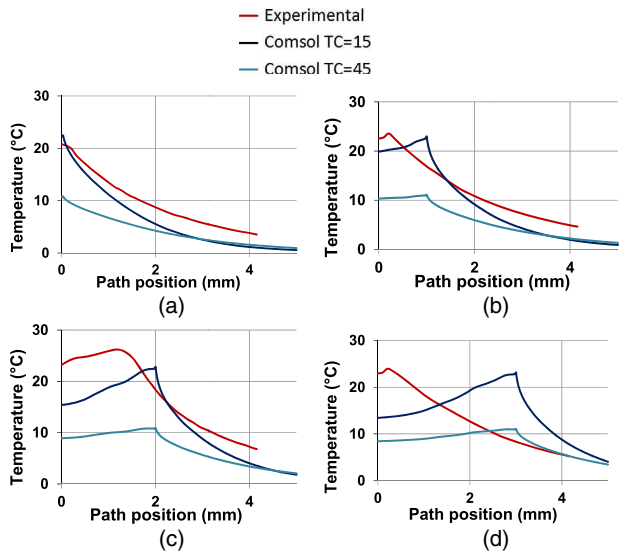

Fig. 14. Comparisons of the temperature profiles along the surface path obtained from experimental measurements and numerical predictions at the 500 ms heating time for: (a) no crack, (b) 1 mm long crack, (c) 2 mm long crack, and (d) 3 mm long crack for the 100 A current intensity.

two current intensities, peak temperature at crack tips followed by a sharp drop in temperature, and high temperature magnitude was created by the high current intensity. Reasons for the discrepancies were presented and discussed in Section 3.A. A noticeable feature found experimentally and numerically is that the temperature drop away from the peak temperature location is faster than that of the straight line coil. Consequently, it is relatively easier to use the loop coil system than the straight line coil system for identifying the peak temperature location. In addition, the peak temperature for the 1, 2, or 3 mm crack is clearly higher than the rest of the temperature variations obtained from the three-loop coil system with the 100 A current intensity. The obtained results showed that the three-loop coil system can effectively detect cracks as small as 1 mm.

Figure 14 also clearly shows that considerable peak temperature shifts exist between the experimental and numerical results, especially for the 3 mm long crack. It has been hypothesized that this shift is mostly caused by the differences in profile between the actual and assumed cracks. To confirm this assumption, additional investigations of the effect of the crack shape on the temperature variation were carried out numerically and the obtained results are presented in the following subsection.

2. Investigation of Peak Temperature Shifts

As discovered from the actual crack profiles in Fig. 11, two evident differences between the actual and assumed cracks are the path orientation and the crack gap. For example, the crack width of the 3 mm crack, shown in Fig. 15, varies significantly over its length with small segments being significantly narrower than others. The small orientation angle was fully covered by the 200 μm pixel size of the IR camera used for measuring temperatures; hence, its effect on the peak temperature location should be ignored. Thus, the remaining possible cause for the shift in temperature location is the variation in crack gap at specific positions along the crack length. This effect of crack width variation on the peak temperature location was studied numerically.

Using the 3 mm crack case for this investigation, four crack scenarios were studied. For those scenarios, the relative permeability was set to 1000, the steel thermal conductivity was set to 15 W/(m K), and a 50 A current intensity was used. The four scenario descriptions are listed below:

- Base condition: continuous crack (without closing);
- Case 1: two crack segments—first segment 0.3 mm, second segment from 0.6 to 3 mm—a 0.3 mm long segment disappeared (no crack) from the position 0.3–0.6 mm;
- Case 2: two crack segments—a 0.3 mm long segment disappeared (no crack) from the position 0.5–0.8 mm;
- Case 3: two crack segments—a 0.3 mm long segment disappeared (no crack) from the position 1–1.3 mm; and
- Case 4: two crack segments—a 0.3 mm long segment disappeared (no crack) from the position 1.5–1.8 mm.

Temperature variations along the prescribed steel surface path are shown in Fig. 16. It can be seen that peak temperatures are always located at the tip of the first crack segment, while the temperature increase found at the tip of the second crack segment is very small and can be negligible. The difference in the temperature levels obtained from the experimental and numerical results should be caused by the steel material parameters used in the models, such as thermal conductivity and others. Good agreement in the peak temperature locations was obtained between the experimental measurements and numerical Case 1 and 2 results, which clearly showed a dominant effect of the crack closing on the peak temperature location. Predictions of Cases 3 and 4 further confirmed that the crack closing condition should be the key reason causing the discrepancy of the peak temperature shifts between the experimental and numerical results. As the crack surface becomes closer, there would be smaller electrical resistance in the current path, and hence, lower heat would be generated. The current study should be

Fig. 15. Microscope image of the 3 mm long crack.

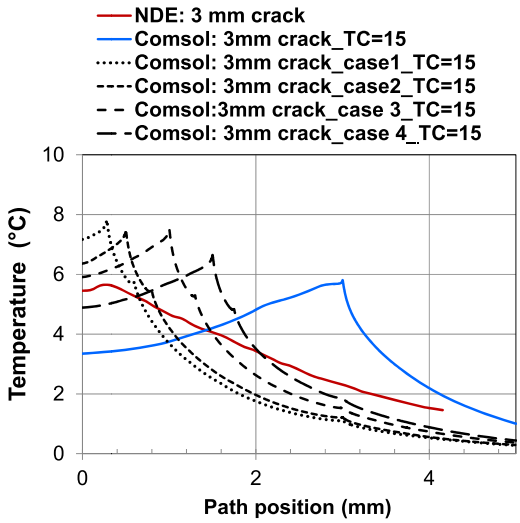

Fig. 16. Comparisons of the temperature profiles along the surface path obtained from experimental and numerical results at the 500 ms heating time for the 3 mm crack in specific conditions for the 50 A current intensity.

a sound base for the implementation of induction thermography for practical assessment of the potential cracks in sizing and flaw detection considering the possible effects of crack geometries in width, closing position, path, etc.

5. DISCUSSION AND COMMENTARY

To support the NDE exploration, 3D finite element models were developed to simulate the induction heating process. Fairly good trend agreement in temperature profiles was obtained between the experimental and numerical results for the steel coupons with different fatigue crack lengths. Temperature comparisons showed a better prediction obtained for the steel with the relative permeability (μ_r) of 1000 and thermal conductivity (k) of 15 W/(m K) than the models with the parameters of $\mu_r = 100$ and $\mathrm{k} = 45\ \mathrm{W/(mK)}$. The developed numerical models supported the NDE induction thermography applications for crack detection in steel coupons. The straight line coil detection capability is limited to cracks 2 mm and longer, while the three-loop configuration was able to detect cracks as small as 1 mm numerically and 0.8 mm experimentally. To further improve the model, more accurate material parameters will be essential as both relative permeability and thermal conductivity variation create a wide range of possible temperature increases.

Based on the obtained results it is recommended that induction thermography inspection of steel parts be performed using a multiple-loop coil system, using at least 100 A current and looking at early heating times, such as 100 or 250 ms. For a same current, the loop configuration generated a thermal contrast over 20 times greater than that of the linear coil configuration. Moreover, an additional differential thermography technique can be very useful to improve the flaw detection and in the case of complex geometry that inherently creates electromagnetic concentration such as in the case of notched coupons, it is essential to perform this additional processing.

Close views of the coupon cracks identified that the actual crack features were different from the idealized ones used in the numerical models. As shown, crack width seems have a significant effect on the peak temperature and thus further investigation of induction thermography for the tight crack would also be advisable. This difference between the actual and assumed cracks is likely the dominant factor to generate the peak temperature shifts between the experimental and numerical results. The inherent complexity of natural cracks versus the idealized crack and its influence on the concentration of electromagnetic field should be another interesting exploration topic, which goes far beyond the scope of the intended work herein. In addition, experiments in steel should be reproduced in a sample without a notch. The notch made it easier to generate controlled crack lengths; however, it concentrated the electromagnetic field and made the inspection scenario less realistic than it would be in most services. To eliminate the influence of the possible crack narrowing and closing on the actual crack detection, it is recommended to use the induction thermography technique being a rapid inspect method for crack detection, and then use a secondary method for flaw sizing measurement.

6. CONCLUSIONS

Both experimental and numerical assessments of the induction thermography technique were conducted for detecting the temperature variation in the notched steel coupons. Effects of the coil system, current intensity, heating time, and crack length on the generated temperature profiles were investigated. With the developed 3D finite element models extra effects of material parameters (relative permeability and thermal conductivity) and crack condition (closing position) were also studied. The numerical results effectively explained the experimental observations on the peak temperature magnitude and position. Discrepancies between the experimental and numerical results in the peak temperature location were identified. Consequently, good agreement in temperature profiles was obtained between the experimental and numerical results. Recommendations on the applications of the NDE technique and numerical modeling were made.

REFERENCES

1. K. J. Kremer, W. Kaiser, and P. Moller, “Das therm-O-matic-verfahren-ein neuartiges verfahren fur die online-prufung von stahlerzeugnissen auf oberflachefeler,” Stahl u. Eisen **105**, 71–76 (1985).
2. G. Riegert, T. H. Zweschper, and G. Busse, “Lockin thermography with eddy current excitation,” Quant. Infrared Thermogr. J. **1**, 21–32 (2004).
3. G. Riegert, T. H. Zweschper, and G. Busse, “Eddy-current lockin-thermography methods and its potential,” J. Phys. IV France **125**, 587–591 (2005).
4. J. Vrana, M. Goldammer, J. Baumann, M. Rothenfusser, and W. Arnold, “Mechanisms and models for crack detection with induction thermography,” Rev. Prog. Quant. Nondestruct. Eval. **27**, 475–482 (2008).
5. J. A. Jankowski, D. P. Johnson, J. D. Jurney, J. E. Freer, L. M. Dougherty, and S. A. Stout, “Experimental observation and numerical prediction of induction heating in a graphite test article,” in *Proceedings of the COMSOL Conference* (2009).
6. L. Cheng and G. Y. Tian, “Pulsed electromagnetic NDE for defect detection and characterisation in composites,” in *IEEE International Instrumentation and Measurement Technology Conference* (2012), pp. 1902–1907.
7. B. Drobenko, O. Hachkevych, and T. Kournyts’kyi, “A mathematical model simulation of high temperature induction heating of electroconductive solids,” Int. J. Heat Mass Transfer **50**, 616–624 (2007).
8. B. Doleman and M. Saad, “Thermal characterization of AS4/3501-6 carbon-epoxy composite,” Front. Heat Mass Transfer **4**, 1–8 (2013).
9. C. Marchand and A. Foggia, “2D finite-element program for magnetic induction-heating,” IEEE Trans. Magn. **19**, 2647–2649 (1983).
10. O. Bodart, A. V. Boureau, and R. Touzani, “Numerical investigation of optimal control of induction heating processes,” Appl. Math. Model. **25**, 697–712 (2001).
11. F. Bay, V. Labbe, Y. Favennec, and J. L. Chenot, “A numerical model for induction heating process coupling electromagnetism and thermomechanics,” Int. J. Numer. Meth. Eng. **58**, 839–867 (2003).
12. M. Louaayou, N. Nait-Said, and F. Z. Louai, “2D finite element method study of the stimulation induction heating in synchronic thermography NDT,” NDT & E Int. **41**, 577–581 (2008).
13. N. Biju, N. Ganesan, C. V. Krishnamurthy, and K. Balasubramaniam, “Frequency optimization for eddy current thermography,” NDT & E Int. **42**, 415–420 (2009).
14. M. Kranjc, A. Zupanic, D. Miklavcic, and T. Jarm, “Numerical analysis and thermographic investigation of induction heating,” Int. J. Heat Mass Transfer **53**, 3585–3591 (2010).
15. Y. S. Huang and J. W. Wu, “Infrared thermal image segmentations employing the multilayer level set method for non-destructive evaluation of layered structures,” NDT & E Int. **43**, 34–44 (2010).

16. M. Omar, M. I. Hassan, K. Satio, and R. Alloo, "IR self-referencing thermography for detection of in-depth defects," Infrared Phys. Technol. **46**, 283–289 (2010).
17. J. Wilson, G. Y. Tian, I. Z. Abidin, S. Yang, and D. Almond, "Pulsed eddy current thermography: system development and evaluation," Insight-Non-Destruct. Test. Cond. Monit. **52**, 87–90 (2010).
18. Y. He, M. Pan, D. Chen, G. Tian, and H. Zhang, "Eddy current step heating thermography for quantitatively evaluation," Appl. Phys. Lett. **103**, 194101 (2013).
19. R. Yang, Y. He, B. Gao, and G. Y. Tian, "Inductive pulsed phase thermography for reducing or enlarging the effect of surface emissivity variation," Appl. Phys. Lett. **105**, 184103 (2014).
20. R. Yang and Y. He, "Eddy current pulsed phase thermography considering volumetric induction heating for delamination evaluation in carbon fiber reinforced polymers," Appl. Phys. Lett. **106**, 234103 (2015).
21. G. Li and M. Genest, "Three-dimensional numerical modelling of induction thermography on metallic panels," in *NDT in Canada Conference Proceedings*, Burlington, Ontario, Canada, November 15–17, 2016.
22. V. Rudnev, D. Loveless, R. L. Cook, and M. Black, *Handbook of Induction Heating* (CRC Press, 2002).
23. F. Mabrouki, M. Thomas, M. Genest, and A. Fahr, "Frictional heating model for efficient use of vibrothermography," NDT & E Int. **42**, 345–352 (2009).
24. M. Genest, M. Martinez, N. Mrad, G. Renaud, and A. Fahr, "Pulsed thermography for non-destructive evaluation and damage growth monitoring of bonded repairs," Compos. Struct. **88**, 112–120 (2009).
25. J. N. Zalameda, W. P. Winfree, J. P. Seebo, and P. H. Johnston, "Thermography inspection for detection and tracking of composite cylinder damage during load testing," AIP Conf. Proc. **1335**, 450–457 (2011).
26. W. P. Winfree, J. N. Zalameda, and P. A. Howell, "Improved flaw detection and characterization with difference thermography," Proc. SPIE **8013**, 80130U (2011).